Hyaluronated mesoporous silica nanoparticles for active targeting: influence of conjugation method and hyaluronic acid molecular weight on the nanovector properties

(Article begins on next page)

01 May 2024

Hyaluronated mesoporous silica nanoparticles for active targeting: influence of conjugation method and hyaluronic acid molecular weight on the nanovector properties

Valentina Ricci[a], Daniele Zonari[b], Stefania Cannito[c], Alessandro Marengo[b], Maria Teresa Scupoli[d], Manuela Malatesta[e], Flavia Carton[e], Federico Boschi[f], Gloria Berlier[a],* and Silvia Arpicco[b],*

[a] Department of Chemistry and NIS Centre, University of Torino, Via P. Giuria 7, Torino, Italy
[b] Department of Drug Science and Technology, University of Torino, Via P. Giuria 9, Torino, Italy.
[c] Department of Clinical and Biological Sciences, University of Torino, Corso Raffaello 30, Torino, Italy
[d] Research Center LURM (University Laboratory of Medical Research), University of Verona, Piazzale L.A. Scuro 10, Verona, Italy
[e] Department of Neurological, Biomedical and Movement Sciences, Anatomy and Histology Section, University of Verona, Strada le Grazie 8, Verona, Italy
[f] Department of Computer Science, University of Verona, Strada le Grazie 15, Verona, Italy

*Co-corresponding authors:
Gloria Berlier
Department of Chemistry and NIS Centre, University of Torino,
Via P. Giuria 7, Torino, Italy
Tel: +39 0116707856
Fax +39 011 6707855
E-mail address: gloria.berlier@unito.
Silvia Arpicco
Department of Drug Science and Technology, University of Torino
Via P. Giuria 9, 10125 Torino, Italy
Tel: +39.011.6706668
Fax +39.011.6706663
E-mail address: silvia.arpicco@unito.

Abstract

We have prepared and evaluated about their the physico-chemical and biological properties of four different hyaluronated mesoporous silica nanoparticles (MSNs) samples (MSN/HA). Hyaluronic acid (HA) with two different molecular weights (200 and 6.4 kDa) was used for the conjugation of aminopropyl-functionalized MSN (NH_2-MSN), following two different procedures. Namely, samples HA200A and HA6.4A were prepared by reacting activated HA with NH_2-MSN (method A), while samples HA200B and HA6.4B were obtained carrying out HA activation in the presence of the nanoparticles (method B). The four samples showed similar hydrophilicity, but clear differences in the HA loading, textural properties, surface charge and stability of the suspensions. More in detail, conjugation using low molecular weight HA with method A resulted in low HA loading, with consequent scarce effects on dispersity and stability in physiological media. The highest yield and corresponding best performances were obtained with method B using high molecular weight HA. HA loading and molecular weight also influenced in a concerted way the biological response towards the MSNs of CD44 target cancer cells (CD44+) and control cells (CD44-): MDA-MB-231 and A2780, respectively. The absence of cytotoxicity was assessed. Moreover, the targeting ability of the best performing MSN/HA was confirmed by cellular uptake studies.
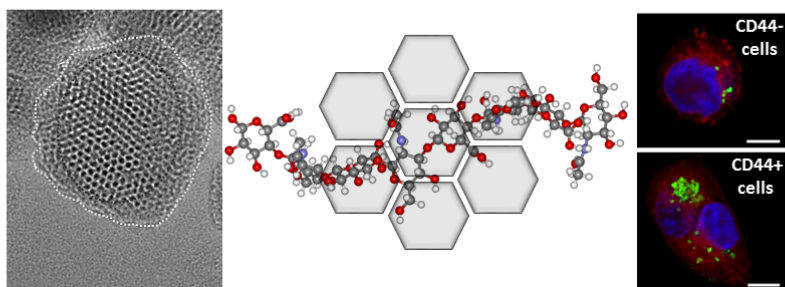
Key words

Hyaluronic acid, mesoporous silica nanoparticles, CD44 receptor, active targeting, hydrophilicity, infrared, water adsorption, MSN

1 **Graphical abstract**

2

3

4 Hyaluronated mesoporous silica nanoparticles (MSN/HA) are preferentially internalized in CD44+

5 tumor cells

6

1. Introduction

Nanoparticles-based targeted therapy has emerged in recent years as an innovative strategy to maintain a drug therapeutic dose at the target site, while reducing systemic drug toxicity and adverse side effects to healthy tissues [1-3]. This approach is particularly important in relation to cancer therapy, where the differences in biochemistry between cancerous and normal tissues can be exploited for the selective targeting of over-expressed tumour specific receptors [4-7]. To this aim, nanomaterials are an ideal playground, thanks to their intrinsic properties such as high surface area, tuneable size and shape coupled to ease of synthesis and functionalization. Nanoparticles may be loaded with a plethora of bioactive molecules (*e.g.*, small molecules, peptides, nucleic acids, etc.) to protect them from cleavage by external agents, thus the encapsulated drugs do not participate in the control over pharmacokinetic and biodistribution. Moreover, nanosize ~~allows for~~ permits passive transport in biological fluids and for establishing molecular interactions at the cellular and subcellular level [1].

Liposomes [8-10] and biodegradable polymeric nanoparticles [11-13] are among the most versatile biocompatible systems to encapsulate active ingredients. Mesoporous silica nanoparticles (MSNs) can be considered as their inorganic counterparts, with intrinsic features such as a huge available inner volume, inertness and chemical stability [14-17]. The ease of surface functionalization makes them ideal materials to develop "pharmaceutically adapted platforms" [18, 19], with great potentiality in relation to *stimuli responsive* applications [20-26]. One of the major drawbacks for the systemic application of these nanosystems is their poor dispersity in biological fluids, which can be however improved by appropriate surface functionalization [19]. Functionalization (often carried out to optimize the interaction with the guest drug molecules) can be obtained with a variety of organosilanes~~, to optimize the interaction with the guest drug molecules~~ [27]. This has important consequences on the surface properties, such as charge and hydrophilicity [28], which ~~in turns~~ can profoundly ~~affect~~ influence ~~the nanoparticle~~ cytotoxicity [29], cellular uptake, transport and/or fate in biological

4

fluids of the nanoparticles [30, 31].

Surface modification of nanocarriers through macromolecules is particularly relevant in the field of cancer treatment [32], where the conjugation of cytotoxic drugs with macromolecules is designed to improve their pharmacokinetic profile, prolonging the distribution and elimination phases [33]. The most employed are N-(2-hydroxypropyl) methacrylamide (HPMA), polyglutamate, human serum albumin, dextrans, heparin, chitosan, dendrimers, multi-arm polyethylene glycol (PEG), and hyaluronic acid (HA) [32, 33]. HA is a naturally-occurring glycosaminoglycan and a major component of the extracellular matrix. The HA receptor CD44 is overexpressed in many cancer cells, and in particular in tumor-initiating cells. HA has thus attracted considerable interest in for the development of nanoplatforms for actively targeting drugs, genes, and diagnostic agents [34, 35].

In recent years, HA-conjugated MSN systems have been proposed in the literature, with the double effect aim to improve the MSNs dispersity and obtain a targeted delivery to CD44 overexpressing cancer cells [36-38]. Zhang *et al*. recently proposed biotin-modified HA coupled to MSN to enable controlled drug release at cancer cells expressing CD44 HA receptor CD44 [39]. Moreover, Chen *et al*. exploited used HA as both capping and targeting agent. In their work, the entrapped guest molecules were released from the inner pores of MSNs upon HA degradation in response to hyaluronidase-1, which occurred after receptor-mediated endocytosis into targeted cancer cells [40]. The potentiality of HA-conjugated MSN systems was further investigated by developing dual-stimuli responsive systems. To this aim, the polysaccharide was conjugated to MSNs through a disulfide bond, which was cleaved in the presence of the high glutathione concentration characterizing cancer cells [23, 24]. Additionally, multifunctional "theranostic" materials where developed, coupling the above-mentioned properties to those of a gadolinium based bovine serum albumin complex for a concomitant simultaneous redox-responsive targeted drug delivery and magnetic resonance imaging [41].

This work reports about In this work, the synthesis and characterization of hyaluronated MSNs (MSN/HA), which have been developed with the double aim to improve their dispersion in physiological media and their targeting ability. Here For the first time we compare different synthetic approaches, and the use of HA of different molecular weights (6.4 kDa and 200kDa), to identify the optimal strategy to obtain the better performances, both in terms of biological response and potential pharmaceutical application. A full physico-chemical description of the produced hybrid materials is given, including routine characterization, hydrophilicity analysis assessment, molecular and quantitative analysis of the HA external shell. Finally, the biological effects in cultured cells were studied and the results correlated to the materials properties.

2. Experimental section

2.1 Materials

Cetyltrimethylammonium bromide (CTAB), tetraethyl orthosilicate (TEOS), sodium hydroxide (NaOH), (3-aminopropyl)-triethoxysilane (APTS) and all the other reagents and solvents were purchased from Sigma-Aldrich (Milan, Italy) and employed as received. Sodium hyaluronate (HA, of molecular weights MW 6.4 and 200 kDa) was purchased from Lifecore Biomedical (Chaska, MN). Fluorescein-5-isothiocyanate (FITC) was provided by Invitrogen (Life Technologies, Monza, Italy). MilliQ® water was used in all synthetic steps.

2.2 NH_2-MSN synthesis

MSN samples were prepared following a slightly modified literature procedure [42, 43]. CTAB (1 g, 2.74 mmol), employed as Structure Directing Agent (SDA), was dissolved in 480 ml of water under stirring and heating. At the stable temperature of 80°C, NaOH (2.0 M, 3.5 ml) was slowly added to the mixture. TEOS (5 ml, 22.4 mmol) was then added dropwise drop-wise over 10 min under vigorous stirring. After 2 h of stirring at 80 °C the milky reaction mixture was cooled to room temperature (RT) and the white precipitate was filtered off and washed with abundant water and

methanol. The SDA was removed from the as-synthesized material by calcination at 550 °C,

heating to the desired temperature under N_2 flow and switching to O_2 for a 6 h isotherm.

Aminopropyl-functionalized MSN (NH_2-MSN) sample was prepared with APTS by post-synthesis

grafting with a procedure modified from the literature [44, 45]. Namely, 1 g of MSN (overnight

dried at 100°C) were suspended in 30 ml of anhydrous toluene. The particles suspension was heated

at 130°C under stirring. Next, 0.6 ml of APTS were added drop-wise and the mixture was allowed

to reflux for 17 h. The modified NH_2-MSNs were filtered off and washed with toluene, ethanol,

water and ~~at last~~ finally methanol. Subsequently, the sample was dried at 110°C for 3 h ~~to favor the~~

for curing, and at 80°C overnight [46].

2.3 Hyaluronic acid conjugation: MSN/HA samples

Conjugation with HA was carried out starting from NH_2-MSN, to exploit the aminopropyl

functionality for covalent linking of the targeting agent. We followed three different procedures

proposed in the literature [36, 37, 40]. The protocol described in Ref [40] was discarded since the

prepared samples resulted in the lowest derivatization yield. This is probably ascribable to the low

concentration of the coupling agent 1-ethyl-3-(3′-dimethylaminopropyl)carbodiimide (EDAC),

notwithstanding the excess of HA with respect to MSN. The methodologies proposed by Yu et al.

and by Ma et al. [36, 37]~~,~~ briefly described below, are hereafter mentioned as method A and B,

respectively. HA of MW of 6.4 and 200 kDa were used ~~with each method~~ for both preparations.

2.3.1 Samples HA200A and HA6.4A

This approach requires activation of HA through N-hydroxysuccinimide (NHS) and EDAC as

coupling agent, before nanoparticles conjugation [37]. To this aim, 56 mg of NHS and 30 mg of

EDAC were separately dissolved in 1.5 ml water, each. 17 mg of HA were suspended in 9 ml water,

before adding the NHS and EDAC solutions previously prepared. The mixture was left under

magnetic stirring at RT for 1 h. 150 mg of NH_2-MSN were suspended by sonication in 15 ml of

water, before adding the activated HA solution. pH was then adjusted to 9 with trimethylamine (TEA). The mixture was heated to 38 °C and left under stirring overnight. After cooling down to RT, the supernatant was separated by centrifugation (60 rpm, 20 min). The solid powdered product was washed thrice with water, and suspended in few ml of water before freeze-drying. This procedure was carried out with HA 200kDa and 6.4 kDa, resulting in samples HA200A and HA6.4A, respectively.

2.3.2 Samples HA200B and HA6.4B

With this method, Following method B, activation of HA was carried out directly in the presence of the nanoparticles. 150 mg of NH_2-MSN were sonicated in 30 ml of 2-(N-morpholino)ethanesulfonic acid (MES) buffer 0.01 M, at pH 6. 150 mg of HA were dissolved in 15 of ml of MES and added to the nanoparticles suspension. 15 mg of EDAC and 15 mg of NHS, each dissolved in 7.5 ml of MES, are were added to the MSN suspension. The reaction was kept under magnetic stirring at RT for 4 h and successively centrifuged (60 rpm, 20 min). After removal of the supernatant, the solid powdered product was washed thrice with water and re-suspended in few ml of water for freeze-drying [36]. The procedure was carried out with HA 200kDa and 6.4kDa, resulting in samples HA200B and HA6.4B, respectively.

2.3.3 Fluorescent labelling

FITC labelled NH_2-MSN and MSN/HA samples were prepared as reported in Ref. [37] with minor modifications. Briefly, 250 µl of FITC ethanol solution (0.3 mg/ml) were added at to a suspension of 1 mg of MSN in 150 µl of water 250 µl of FITC ethanol solution (0.3 mg/ml) were added. The mixture was maintained at RT for 6 h under stirring in the dark and then the nanoparticles were centrifuged (60 rpm, 10 min) and washed with ethanol thrice until the supernatants were colorless.

2.4 Physico-chemical characterization

~~High Resolution~~ Transmission Electron Microscopy (~~HR~~TEM) ~~analyses were performed by means~~ ~~of~~ measurements were carried out with a JEM 3010-UHR microscope (JEOL Ltd.) operating at 300 kV. ~~For the measurements, p~~ Powders were dispersed on a copper grid coated with a perforated carbon film. The size distribution of the samples was obtained by measuring a statistically representative number of particles (*ca.* 250 particles).~~and the~~ The results are indicated as mean particle diameter (dm) ± standard deviation (STD) (dm±STD).

Specific surface area (SSA), cumulative pore volume and pore size distribution of samples were calculated by gas-volumetric analysis measuring N_2 adsorption-desorption isotherms at liquid nitrogen temperature (LNT) using an ASAP 2020 physisorption analyser (Micromeritics). The SSA was calculated by the Brunauer-Emmett-Teller (BET) method and the average pore size was determined by means of the Barrett-Joyner-Helenda (BJH) method, employing Kruk–Jaroniec–Sayari (KJS) equations on the adsorption branch of nitrogen isotherms. Before the measurement, the samples were outgassed at RT overnight.

Powder X Ray Diffraction (~~P~~XRD) patterns were collected with a PW3050/60 X'Pert PRO MPD diffractometer (Panalytical) working in Bragg–Brentano geometry, using Cu Kα radiation (40 mA and 45 kV), with a scan speed of $0.0167°$ min^{-1} and a measure time of 200 s/step. The measure was carried out at low angles, in the range of 1.5-12°.

Thermogravimetric analysis (TGA) was carried out on a Q600 analyzer (TA Instruments) heating the samples at a rate of 10 °C/min from RT to1000°C in air flow. Before starting measurements, samples were equilibrated at 30°C.

Fourier Transform Infrared (FTIR) spectra were recorded using an IFS28 spectrometer (Bruker Optics) equipped with a MCT detector, working with a resolution of 4 cm^{-1} over 64 scans. The spectra were obtained in transmission mode, with ~~the~~ samples pressed in the form of self-supporting pellets, mechanically protected with a pure gold frame. Samples were placed in quartz cells equipped with KBr windows, allowing *in situ* activation and measurement. Before spectra measurement the samples were outgassed at RT for 4 hours to remove adsorbed water and

impurities. Spectra were normalized with respect to pellet thickness for direct comparison, by using the silica overtone modes in the 2100-1500 cm^{-1} interval.

Colorimetric carbazole test was carried following the procedure described in [47]. Briefly, a suspension of 4 mg/ml in water was prepared for each sample. Two aliquots (60 and 180 µl) were diluted to a final volume of 1 ml in water. 3 ml of a 0.025 M $Na_2B_4O_7$·in H_2SO_4 96% solution were added to each tube. The suspensions were then shaken and heated at 100°C for 10 min. After cooling down, 100 µl of a carbazole solution 0.1% p/v in absolute ethanol was added, before mixing and heating again at 100°C for 10 min. After cooling down, absorbance was measured at 530 nm using a DU-70 Beckman spectrophotometer.

Microgravimetric H_2O adsorption/desorption isotherms were measured with an intelligent gravimetric analyzer (IGA-002, Hiden Analytical), based on an ultrahigh-vacuum (UHV) microbalance (weighing resolution of 0.2 µg) with integrated temperature and pressure control. Temperature control was based on a thermostated water bath/circulator, while pressure control was achieved with a Baratron capacitance manometer (accuracy ± 0.05 mbar). Buoyancy corrections were carried out using the weights and densities of all the components of the sample (including adsorbed phase) and counterweight sides of the balance, and the measured temperature. The mass uptake was measured as a function of time, and the approach to equilibrium of the mass relaxation curve was monitored in real time using a computer algorithm (real time processor, RTP). For each isotherm point the time origin of real-time analysis was set at 75% of the pressure change, while the minimum and maximum data collection time were set to 5 and 60 mins, respectively. RTP uses last-squares regression of a linear driving force (LDF) model in order to extrapolate a value of the mass relaxation asymptote and assess the time-scale of interaction. The samples were loaded in a sealed stainless steel reactor, where they were outgassed at 50°C overnight prior to H_2O dosage, in order to measure the sample dry weight. Two consecutive adsorption/desorption isotherms were measured varying the water equilibrium pressure in the 0-20 mbar interval (step of 3 mbar) at 28 °C. This corresponds to a maximum p/p^0 value around 0.55 ($p^0 \cong 38$ mbar at the measurement temperature).

The experimental isotherms were analyzed with a Langmuir model, which assumes a monolayer adsorption onto the surface and is expressed by the equation:

$$q = \frac{q_m K \, p}{1 + K \, p} \qquad (1)$$

where q is the equilibrium water uptake, q_m is the adsorption capacity (corresponding to the monolayer saturation) and K the Langmuir constant, which corresponds to the adsorption equilibrium constant [48]. q_m and K were calculated via the linearization of the Langmuir equation, as follows:

$$\frac{p}{q} = \frac{1}{K \, q_m} + \frac{p}{q_m} \qquad (2)$$

Calculations were carried out expressing the equilibrium pressure as p/p^0, so that the K values reported in Table 4 are dimensionless.

The mean hydrodynamic size was determined at 25°C by Dynamic Light Scattering (DLS) using a nanosizer (Nanosizer Nano Z, Malvern Inst., Malvern, UK). The selected angle was 173° and the measurement was ~~taken~~ carried out after dilution of the nanoparticle suspensions in water and in phosphate buffered saline (PBS 0.1 M, pH = 7.4). The particle surface charge was investigated by zeta potential measurements at 25°C in water and PBS solution applying the Smoluchowski equation and using the ~~NanosizerNanoseries~~ Zetasizer Nanoseries ZS 90 (Malvern Instruments~~.~~). In both cases, measurements were carried out in triplicate by diluting 80 μl of a 1mg/ml particles suspension in water with the selected medium, to reach a final volume of 1 ml.

For the dispersity test 2 mg of NH_2-MSN and MSN/HA samples were added to 1 ml of different medium [PBS 0.1 M or Dulbecco's Modified Eagle Medium (DMEM) supplemented with 10% of fetal bovine serum (FBS)] and bath sonicated for 30 min. ~~then dispersity~~ The stability of the dispersions was evaluated after 0, 4, 8, 24 and 30 h ~~was evaluated~~.

2.5. Tumour cell lines culture

11

MDA-MB-231 (human breast adenocarcinoma) and A2780 (human ovarian carcinoma) cells were used. MDA-MB-231 cells were grown in DMEM supplemented with 10% of FBS, 0.03% of L-glutamine and 2% penicillin and streptomycin. A2780 cells were cultured in RPMI 1640 medium containing 10% FBS, 0.03% of L-glutamine, 2% penicillin and streptomycin, and 50 g/ml of gentamicin sulfate. Cells were maintained in a humidified incubator at 37°C in 5% CO_2.

2.6. Receptor expression analysis

Flow cytometry was used to determine the presence of CD44 on the cell surface by indirect immunofluorescence. Cells were washed twice with PBS and incubated 30 min in the dark at 4 °C with CD44 primary antibody, washed twice with PBS and then incubated 30 min in the dark at 4 °C with a phycoerythrin (PE) conjugated goat antibody (Dako Italia, Milan, Italy). Samples were analyzed on a flow cytometer instrument (FACSCanto, Becton Dickinson, San Jose, CA). Dead cells and debris were excluded on the basis of forward-scatter and side-scatter. Flow cytometry data were analyzed using the FlowJo software (TreeStar, Ashland, OR). CD44 expression was measured by calculating the ratio between median fluorescence intensity of cells labelled with antibodies versus unlabelled cells (Relative Median Fluorescence Intensity, RMFI).

2.7. Incubation with MSN and cytotoxicity evaluation

MDA-MB-231 and A2780 cells were seeded at 1 x 10^4 cells/well in 96 wells microtiter plates and incubated overnight to allow cellular adhesion. Various dilutions of NH_2-MSN and MSN/HA samples (1.5-25 µg/ml) were added in triplicate, and incubated for 24, 48 and 72 h.

Cell growth inhibition was evaluated by sulforhodamine B (SRB) colorimetric proliferation assay, modified by Vichai and Kirtikara [49].

2.8 Confocal analysis of fluorescent MSN

After 24 h incubation with either FITC labelled NH_2-MSN or MSN/HA, MDA-MB-231 and A2780 cells were fixed for fluorescence microscopy with 4% (v/v) paraformaldehyde in PBS, pH 7.4, for 30 min at room temperature. The samples were stained for DNA with Hoechst 33342 (1 µg/ml in PBS for 5 min; Sigma), counterstained with 0.1% Trypan blue in PBS for 30 sec to visualize the cytoplasm, rinsed in PBS, and mounted in a 1:1 mixture of glycerol:PBS (Calbiochem, Inalco, Milan, Italy). For confocal laser scanning microscopy (CLSM), a Leica TCS SP5 AOBS system (Leica Microsystems Italia, Milan, Italy) was used with a 40x oil immersion objective. For fluorescence excitation, a diode laser at 405 nm for Hochest, an Ar laser at 488 nm for FITC and a He/Ne laser at 543 for Trypan blue were employed. Z-stack of 1.5 µm step sized images (each image in the 1024x1024 pixel format) were collected and processed by the Leica confocal software. The RGB channels of the images presented here are the gray intensity images obtained with 405 nm (B), 488 nm (G) and 533 nm (R) excitation wavelengths respectively.

2.9 Cellular uptake

A quantitative determination of the cellular uptake was performed on a fluorescence-activated cell sorter (FACS). MDA-MB-231 and A2780 cells seeded in 6-well culture plates ($5X10^5$ cells/well), were exposed for different length of time (15 min, 30 min or 1 h) to FITC labelled NH_2-MSN and MSN/HA with equivalent fluorescence. After removal of the free FITC-NH_2-MSN and FITC-MSN/HA, cells were washed twice with PBS, collected by tripsynization and finally re-suspended in 1 ml of PBS. Then the intracellular uptake of MSNs was analyzed using a FACScan. Detection of FITC-MSNs green fluorescence (FL-1) was performed on at least 5,000 events per samples, using the CellQuest software (Becton-Dickinson, Milano, Italy). Cells incubated in the absence of MSN were used as control.

3. Results and discussion

All samples were characterized about their general properties, The general properties of all samples, including textural and morphological features, were analyzed. Sample HA6.4A was discarded due to low derivatization yield and to scarce dispersity (see later), and will thus not be described in detail in the following. The NH$_2$-MSN sample used for HA conjugation was measured for comparison. Corresponding results are hereafter discussed only when relevant.

3.1 Effect of conjugation on porous structure

MSN/HA samples are composed by spherical nanoparticles (particle size 94±20 nm, see corresponding histogram as Figure S1), which are characterized by an ordered pore structure with the typical hexagonal array of MCM-41-like materials. This can be appreciated in the high resolution TEM picture of sample NH$_2$-MSN, reported in Fig 1a, showing two superimposed particles with pores parallel and perpendicular to the image plane (circle and hexagon shapes, respectively). The same particle size, morphology and ordered porosity is are preserved after HA conjugation, as shown in Figures 1b-d. However, in this case an amorphous-like external layer is clearly observed, which can be attributed to the formation of a shell of HA, covering the particles. The formation of a HA shell is supported by both qualitative and quantitative characterization results, described in the following.

The ordered pore structure of the materials is also reflected in the typical XRD pattern, characterized by low angle peaks at 2.3, 4.0 and 4.7° (Figure S2). These can be labelled as (100), (110) and (200) in the P6mm symmetry group, corresponding to the a hexagonal pore array of pores. After HA conjugation, in all samples the peaks decrease in intensity and move to slightly higher 2θ values in all samples. The change is in the order HA200A < HA6.4B ≅ HA200B. Both phenomena are usually observed in MCM-41-like materials after functionalization and/or drug encapsulation, and are interpreted in terms of molecules filling/lining the pores [50, 51]. Particularly, the d$_{100}$ parameter, which is the distance between planes passing through the pores

centre (see Figure S3), can be calculated from the Bragg equation, as resumed in Table 1. These

data are further discussed hereafter in combination with results from gas-volumetric analysis.

The nitrogen adsorption/desorption isotherms of the three MSN/HA and parent NH_2-MSN materials

are reported in Figure 2 (top panel), with the corresponding pore size distribution calculated with

the BJH method (bottom). Curves a) and b), corresponding to NH_2-MSN and HA200A, can be

classified as type IV, typical of mesoporous materials. Namely, a steep increase of the adsorbed

amount is observed below $p/p^0 = 0.3$, which corresponds to the capillary condensation of the

adsorbate inside the pores. The narrow hysteresis loop present in all samples at p/p^0 reaching 1 is

instead related to condensation of nitrogen in the interparticle porosity. After conjugation, the

nitrogen adsorbed amount decreases in the order HA200A > HA6.4B $\cong$ HA200B, and in the latter

last two the capillary condensation related to mesopores filling is no more present. This is reflected

in the corresponding pore size distribution curves (Figure 2, bottom panel). Parent NH_2-MSN

material shows an intense and relatively narrow peak centred around 30 Å, corresponding to the

pores lined with aminopropyl groups. This peak is weaker and shifted to lower values for HA200A,

very weak and not present for in HA6.4B and HA200B, respectively.

The textural parameters obtained from these data are summarized in Table 1. On the whole, we

observe a major effect of conjugation on samples prepared by method B, where Specific Surface

Area (SSA), pore volume and diameter are sensibly decreased. This suggests that during this

procedure (where HA activation is carried out directly in the presence of the nanoparticles) the

polymer is not only forming an external layer but it is also diffusing inside the pores. This is less

likely in the case of high molecular weight HA, where the polymer could mainly block pores

entrance not allowing nitrogen molecules to diffuse within during BET measurements. On the other

hand, method A, where HA activation is carried out before reaction with NH_2-MSN, results in a

minor diffusion inside the pores, which are less obstructed to the diffusion of the nitrogen adsorbate

used for gas-volumetric analysis. These considerations are in very good agreement with XRD and

TEM observations, showing an apparently thicker HA layer on sample HA200B with respect to the

other two (compare Figure 1b with c and d). Finally, the mean pore diameter calculated by BJH method was combined with the *a* parameter calculated from XRD (distance between centres of the pores, see Figure S3), to calculate the apparent wall thickness. The values, summarized in last column of Table 1, clearly show an increase in the order HA200A < HA6.4B $\cong$ HA200B, in agreement with the above considerations.

3.2 Quantitative HA analysis

Quantification of HA ~~bonded~~ <mark>covalently linked</mark> to the NH$_2$-MSN particles was carried out by two independent techniques, namely TGA and the carbazole colorimetric test.

TGA was carried out from 30 to 1000 °C in air flow, in order to quantify the amount of organic groups anchored to the silica surface. This was calculated on the basis of the observed weight loss, normalized to the dry mass of the sample, *i.e.* after removal of physisorbed water around 100 °C (Figure S4). All MSN/HA samples show a consistent weight loss between *ca* 180 and 650 °C, which is higher with respect to parent NH$_2$-MSN, in the order HA200A < HA200B $\cong$ HA6.4B. The calculated amounts are summarized in Table 2. More details about the criteria used for quantification can be found in the Supplementary Material. In this context, it is sufficient to mention that samples HA200B and HA6.4B show very similar weight losses and curves slope, while HA200A has an intermediate profile, both in terms of quantity and curve shape, in very good agreement with the trends observed with textural and structural techniques, as described above.

Carbazole colorimetric test was also employed for HA quantification. As mentioned above, HA is a high molecular weight glycosaminoglycan, formed by a repeating disaccharide unit composed by D-glucuronic acid and *N*-acetyl-D-glucosamine. In this test HA is hydrolyzed in acid environment, so that monosaccharide units can form coloured adducts with carbazole through their glucuronic acid residues. This allows the quantification of HA through a simple optical measurement.

The values obtained with both techniques are resumed in Table 2, expressed as HA weight percentage. First of all, we underline the very good agreement between the two techniques.

16

Secondly, the results show that a definitely higher mass of HA has been linked to MSN with method B, irrespective of its molecular weight. Method A definitely yields a materials with lower (around one third) HA loading. This could be explained by the fact that in the latter case HA activation was carried out before reaction with NH_2-MSN. On the basis of gas-volumetric and TEM results, we infer that this could result in a more difficult diffusion inside the pores, so that mainly external aminopropyl groups were involved in the reaction. Finally, these results contribute to the interpretation of the structural and textural parameters of the MSN/HA samples, which appear to be mainly affected by the HA loading, irrespective of its molecular weight.

3.3 Qualitative HA analysis: infrared spectroscopy

Infrared spectroscopy is a powerful tool to investigate interface interactions in hybrid organic-inorganic materials. It can be used to assess the molecular structure of surface grafted functionalizing groups, and the weak interactions taking place between silica surface and adsorbed/encapsulated drug molecules [28, 50-58]. The spectra of parent NH_2-MSN and HA conjugated samples are reported in Figure 3, in the high and low frequency ranges (top and bottom panel, respectively). All samples were measured in transmission mode on self-supporting pellets, after RT evacuation necessary to remove adsorbed impurities and water, which would influence the spectral analysis (see for instance Refs. [28] and [57]). The spectrum of HA 200 kDa (measured in KBr) is reported for comparison in the Supplementary Material (Figure S5). The bands assignment discussed in the following is resumed in Table 3.

The spectrum of parent NH_2-MSN sample, reported for comparison, is similar to what already reported and discussed in the literature [28, 57]. Namely, it is characterized by a broad signal in the high frequency region (top panel), which is characteristic of hydrogen bonding interactions among surface Si-OH groups (silanols) and between these and the grafted aminopropyl functionalities. The presence of the aminopropyl groups is testified by the ~~components~~ bands (superimposed to the broad band described above) at 3370 and 3300 cm^{-1} (antisymmetric and symmetric NH_2 stretching

1   modes, νNH_2, respectively) and at 2930/2870 cm^{-1} (antisymmetric and symmetric νCH_2). The very

2   weak peak at 3734 cm^{-1} is related to hydrogen bonding acceptors and/or ~~germinal~~ geminal -Si(OH)$_2$

3   silanols, which were not consumed by the grafting reaction [57]. The corresponding fingerprints of

4   aminopropyl functional groups in the low frequency region (bottom panel of Figure 3) are the band

5   at 1595 cm^{-1} due to the NH$_2$ bending mode (δNH_2) and the weak δCH_2 features between 1500 and

6   1320 cm^{-1}.

7   The spectra of MSN/HA samples show interesting differences with respect to parent materials.

8   Namely, in the high frequency region an increase in the intensity and spectral breadth of the

9   absorption between 3700 and 2200 cm^{-1} is observed, in the order HA200 < HA200 B $\cong$ HA6.4B.

10   This can be clearly related to the presence of an extended hydrogen bonding network, both among

11   HA residues and between them and the silica surface. Indeed, the weak band at 3734 cm^{-1} related to

12   Si-OH groups is consumed, confirming the involvement of surface silanols in hydrogen bonding

13   interactions with HA.

14   Moreover, weak ~~components~~ bands can be also observed between 3200 and 3000 cm^{-1}, recalling the

15   typical spectral shape of hydrogen-bonding carboxylic acids. This indicates that not all the D-

16   glucuronic acid residues were involved in the formation of an amidic bond with the amino groups

17   present on silica. In agreement with the structural, textural and quantitative data discussed above,

18   the two samples prepared by method B are very similar and more affected by conjugation, at

19   variance with sample HA200A, showing an intermediate behavior.

20   The same trend is observed in the low frequency range (Figure 3, bottom panel). More in detail,

21   broad absorptions develop in the 1700 – 1500 cm^{-1} and 1450 - 1350 cm^{-1} ranges, with the same

22   order of intensity described above, *i.e.* HA200 < HA200 B $\cong$ HA6.4B. The δNH_2 signal at 1595 cm^{-1}

23   ^{1} is clearly evident on sample HA200A, ~~and as~~ while it is only a shoulder in the other samples. This

24   indicates that not all aminoproyl functionalities reacted with HA, as expected for functional groups

25   lining the inner surface of the pores. Interestingly, the intensity of this band is higher on sample

1   HA200A, where a lower diffusion of HA residues inside the pores was inferred from textural and

2   structural analysis (see above).

3   Concerning the new ~~spectral~~ features developing in this spectral region after HA conjugation, they

4   can be safely ascribed to the formation of an amidic bond between the NH_2-MSN amino groups and

5   the carboxylic acid functionalities of HA. Namely, the amide I band (νCO) is observed at 1650 cm⁻

6   ¹, the amide II (δNH and νCN combination mode) at 1550 cm⁻¹, while the absorption between 1430

7   and 1350 cm⁻¹ is related to the numerous δCH and δOH vibrations of HA.

8

9   *3.4 Interaction with water molecules*

10   HA is a hydrophilic macromolecule, with interesting applications as wetting agent [59-61] or as

11   polymer for surfaces modification. Indeed, recent studies reported about the use of HA to improve

12   hydrophilicity and biocompatibility of chitosan films or scaffolds [62, 63]. Moreover, HA has been

13   used to increase surfaces hydrophilicity to provide antifouling properties, as a result of reduced

14   nonspecific protein adsorption [64-68]. In this work, the effect of HA conjugation on the

15   hydrophilic character of MSN has been studied by carrying out water vapour sorption

16   microgravimetric experiments. This technique has been recently employed by some of us to

17   investigate the effect of different functional groups on the hydrophilic character of MSN [28].

18   Water adsorption/desorption isotherms at 28 °C were measured on the three MSN/HA, by gradually

19   increasing the equilibrium vapour pressure in the 0- 20 mbar range (p/p^0 from 0 to ca 0.55). The

20   results obtained on sample HA6.4B are reported in Figure 4 (top panel). Similar trends were

21   observed on samples HA200A and HA200B (see Figure S6) and can be summarized as follows.

22   Both primary and secondary adsorption/desorption cycles are characterized by a hysteresis loop,

23   with higher water uptake measured during the desorption step, for each p/p^0 value. This can be

24   explained by the slow diffusion of water interacting with the external HA layer surrounding the

25   MSN. This implies that the equilibrium is probably not reached in the adsorption step within the

26   time frame of the experiment (timeout of 60 minutes for each p/p^0 dosage). A small water amount is

not desorbed after the first desorption step, and in all samples the second cycle results in a slightly higher water uptake. When comparing the secondary desorption curves on the three MSN/HA samples, the following order of water uptake is observed: HA6.4B > HA200A $\cong$ HA200B (Figure 4, bottom panel).

The obtained results are at first sight surprising, when compared to what measured on the parent NH_2-MSN material, where a maximum uptake of 6.7 wt% (3.7 mmol/g) was measured at $p/p^0 \cong 0.3$ and 25 °C [28]. This is sensibly higher with respect to what obtained on the MSN/HA samples (1.3-1.7 wt%, see Table 4), indicating a decrease ~~of~~ in the water uptake of MSN after HA conjugation, in contrast to what expected for the high hydrophilicity of the polysaccharide. However, the explanation of this apparently puzzling results can be found through a more detailed analysis of the measured isotherms. To this aim, the primary and secondary desorption curves of the samples have been fitted with a Langmuir model, assuming that they are closer to the thermodynamic equilibrium with respect to adsorption ones. The results from this analysis are summarized in Table 4, together with the results for NH_2-MSN parent sample (data from Ref. [28]). First, we acknowledge the fact that for all HA conjugated samples the agreement with the Langmuir model is satisfactory ($R^2 >$ 0.99), which is not the case for NH_2-MSN ($R^2 = 0.9267$ for both cycles). Secondly, the set of calculated K values (corresponding to the equilibrium constant of the adsorption process) are consistent for the set of samples, ranging from 17 to ca 23, while for NH_2-MSN a value around 8.5 was found for both sorption cycles. These data clearly indicates that on the conjugated samples water is mainly interacting with the external HA layer, where it is strongly adsorbed and cannot freely diffuse inside the MSN pores, at least in the time frame and experimental conditions of the experiment. This picture fits well with the higher K values and smaller uptake with respect to parent NH_2-MSN.

Coming back to the comparison among the three samples (Figure 4, bottom panel) the calculated K values are in the order HA200A < HA200B < HA6.4B. The last samples being the one with the highest uptake, we can infer that the polysaccharide molecular weight influences its hydrophilicity.

On the contrary, water uptake on HA200A is almost identical to HA200B, irrespective of the different loading. This supports the idea that, when dosed from vapour phase, water is strongly adsorbed on the external HA layer with limited diffusion within the pores. This effect could limit the diffusion of drugs to and from the material pores, as indicated by preliminary studies on drug loading carried out in our group (not reported). Noticeably, samples HA200B and HA6.4B shows a similar water/HA weight ratio (ranging from 0.07 to 0.09) with respect to the sample prepared by method A (0.21-0.22). These data further support the picture obtained by characterization techniques, indicating that sample HA200A is characterized by a different distribution of HA at the pores entrance, with a consistent amount of unreacted amino groups. This could indicate an easier diffusion of adsorbates (such as water molecules) and host drug molecules within the sample.

3.3 Effect of HA on surface charge, aggregation and dispersity

The electrophoretic mobility of the materials was measured to evaluate the effect of conjugation on the particles ζ potential, which gives an indirect information about the surface charge in the Stern layer. This parameter is affected by both the hydrodynamic diameter and the electric double layer thickness, the latter being strongly influenced by the fluid ionic strength and pH. An estimation of the double layer thickness as a function of the ionic strength can be used in the Henry equation, to convert electrophoretic mobility into ζ potential values [69]. However, in this work ζ potential values (summarized in Table 2) were calculated with the Smoluchowski equation (representing an approximation valid for thick double layers), for direct comparison with the literature works in the field [28, 70-73].

In aqueous solution, the amine group is positively charged while the carboxylic ones of HA show a negative charge in relation to their pKa. Assessing the pKa of both covalently linked HA external layer and aminopropyl groups is not straightforward, since both systems are intrinsically complex. Indeed the pKa of amino-functionalized hybrid materials ~~is~~ has been the subject of extensive research work, since the covalent bond and interactions with the inorganic surface can affect the

amino basicity [28, 57, 74-78]. In our work, ζ potential values in water change depending on the amount and on the molecular weight of the conjugated HA. At equal HA molecular weight (compare HA200A and HA200B, 2nd and 3rd lines in Table 2), the ζ potential decreases as the amount of HA increases. Namely, HA200A (HA loading 6.6 wt%) shows a small but positive value (+14.3 ± 1.3 mV), while HA200B, with a HA loading almost triple is characterized by a negative ζ potential (-19.8 ± 1.9 mV). Samples obtained by method B showed a more negative surface charge; in fact, according to TGA and carbazole test, this method allows a more efficient conjugation.

Considering the different HA molecular weights of samples obtained by the same conjugation method, HA200B showed a more negative surface charge with respect to HA6.4B, without clear correlation with the HA loading. Measurements were also carried out on sample HA6.4A, which was discarded for a more detailed characterization because of low HA loading (3.1 wt% as measured by carbazole test, see Table 2) and scarce dispersity (see below). Indeed, this sample shows a ζ potential value in water almost identical to NH_2-MSN, in agreement with the low derivatization yield.

When the same measurements are carried out in PBS, a different trend is observed, in that almost all samples show more negative ζ potential values. As recently reported, buffer ions can strongly affect adsorption phenomena at the solid-liquid interphase of charged nanoparticles [73, 79, 80]. Marucco *et al*. pointed out how adsorption of phosphate ions from the buffer solution can influence the particles surface properties and charge [79]. On the other hand, we cannot exclude the competition of chloride (and Na^+ and K^+ cations, although at a lesser extent) in modifying the effective surface charge of MSNs, in agreement with the work by Cugia et al. [73]. Indeed, in our work all the three considered HA conjugated samples show a similar negative ζ potential value (around -16 mV), irrespective of the values measured in water. On the contrary, parent NH_2-MSN still shows a positive (though minor) charge and sample HA6.4A is almost neutral (-1.3 ± 0.5 mV).

These results cannot easily be rationalized due to the complex interactions of buffer ions with nanoparticles [73].

DLS measurements were carried out to estimate the hydrodynamic sizes of all samples in both water and PBS (Table 2). The average values are always higher than the size of the single particles measured by TEM, indicating agglomeration. A slight decrease in the size is observed after HA conjugation, particularly for high molecular weight and loading, indicating a positive effect of the polymer against the MSNs tendency to agglomeration. Since our attention is focused on the possibility to use these systems for pharmaceutical application, we have followed the evolution of the hydrodynamic size with time. Figure 5 shows the results obtained on the more stable samples in PBS, *i.e.* HA6.4B, HA200A and HA200B. ~~All~~ The samples show a slight increase of dimensions in the first hours, and then reach a stable value, apart from sample HA6.4B which is characterized by larger size and lower stability. These observations are reflected in the dispersity tests described below.

The pictures acquired during dispersity tests in PBS are shown in Figure 6. In this case a higher concentration was used (2 mg/ml *vs* 0.08 mg/ml used for both ζ potential and DLS measurements), for easier visual observation. The samples with HA of higher molecular weight were better dispersed with respect to parent NH_2-MSN and HA6.4B, which started to precipitate after 4 h. On the contrary, dispersity was dramatically improved after conjugation with high molecular weight HA: HA200A and HA200B formed a stable suspension in PBS for more than 24 h. The enhanced stability of these samples can be explained on the basis of their steric hindrance and of the electrostatic repulsion among the stretched hydrophilic HA chains, reducing the possibility of agglomeration and precipitation. Finally, as concern sample HA6.4A, its precipitation is already complete ~~already~~ after 4 hours, in agreement with a ζ potential value close to zero~~measured almost zero charge~~. The dispersity tests carried out in DMEM +10% FBS showed a similar trend (data not reported).

These data confirm the working hypothesis that HA conjugation is a simple and effective method for improving the dispersity and stability of the nanoparticles, which is in turn beneficial for blood circulation making ~~the further~~ intravenous injection possible. Moreover, our study points out how, irrespective of the similar measured ζ potential, which is influenced by the chemical nature of the buffer medium, the molecular weight of the conjugating macromolecule has a strong influence on dispersity.

3.4 Biological characterization

3.4.1. Analysis of cell surface CD44 expression

The HA receptor CD44, an ubiquitous transmembrane molecule, is expressed at low levels on the surface of several normal cells and overexpressed in many cancer cells [81]. The levels of receptor cell surface expression were preliminary evaluated on a panel of cancer cell lines (MDA-MB-231, JR8, A459, MCF7 and A2780) using anti-CD44 antibody and flow cytometry, with the aim to identify the cell models to be used for further *in vitro* studies. The results show that A2780 cells did not express detectable amount of CD44 whereas MDA-MB-231 cells display a very high expression (Figure 7). Thus, to evaluate the cytotoxic activity and the cellular uptake of the nanoparticles, MDA-MB-231 and A2780 cells were chosen as CD44+ and CD44- cancer cells, respectively.

3.4.2 In vitro cytotoxicity

The *in vitro* cytotoxicity of NH$_2$-MSN and MSN/HA was evaluated after treatment of 24, 48 and 72 h in the concentration range of 1.5-25 µg/ml. ~~and~~ The results showed that the nanoparticles were non-toxic for both cell lines demonstrating the good safety and biocompatibility of the carriers (data not shown). These data are in agreement with the results obtained with other HA decorated MSN [24, 36, 37, 40].

3.4.3 In vitro targeting analysis

Efficient cellular uptake is a major requirement for the therapeutic efficacy of nanoparticles targeting. To test the targeting ability of our MSN we evaluated the cellular uptake of both FITC-labelled NH_2-MSN and MSN/HA on MDA-MB-231 (CD44+) and A2780 (CD44-) cell lines by both CLSM and FACS.

CLSM allowed us to visualize ~~visualizing~~ the cellular uptake and biodistribution of the nanoparticles ~~by~~ in these two cell lines. As shown in Figure 8, in both cell lines MSN occurred in the cytoplasm as clusters of different size; accordingly, previous TEM studies ~~at transmission electron microscopy~~ demonstrated that these nanoparticles are internalized by the cell via both endocytosis and phagocytosis, and then accumulate into cytoplasmic vacuoles [82]. Moreover, MSNs were never found inside the nucleus of MDA-MB-231 and A2780 cells, consistently with previous observations ~~in the same or in different cell lines treated with these nanoparticles~~ [23, 24, 40, 82-85]. Although CLSM does not allow precise quantitation of cellular uptake, the amount of internalized NH_2-MSN was apparently similar in the two cell lines, whereas HA6.4B and HA200B were more abundant in MDA-MB-231 than in A2780 cells. This suggests that MSN/HA possess significant selectivity for cells overexpressing CD44 receptors, ~~consistently~~ in agreement with our results obtained with flow cytometry (see below).

In addition, microscopic observation of the samples revealed the absence of evident morphological alterations in both cytoplasm (e.g. vacuolization) and nucleus (e.g. pyknosis, apoptosis), thus confirming the high biocompatibility of NH_2-MSN and MSN/HA at the concentrations tested in this study.

The morphological images obtained by CLSM are consistent with the flow cytometry analysis performed in order to obtain a quantitative comparison between FITC labelled NH_2-MSN and MSN/HA ~~nanoparticles characterized by different preparation methods and different HA molecular weight~~ (Fig. 9). After treating A2780 and MDA-MB-231 cells with the different MSN/HA, their uptake in A2780 cells is moderately increased in a time dependent ~~depending~~ manner, but almost

irrelevant in comparison with MDA-MB-231 (Fig. 9A). In particular, the FITC mean intensity of MSN/HA200 (both A and B) was dramatically increased in MDA-MB-231 in comparison to A2780 (Fig. 9A, B). Concerning MDA-MB-231, we observed that the cellular uptake efficiency is increased over incubation time (up to 1h, when the uptake is near plateau, approximately 80%, Fig. 9C). Moreover, the cellular uptake efficiency is also dependent on the amount of HA on nanoparticles surface and on its molecular weight. In particular, we obtained a higher uptake of HA200B versus HA200A, demonstrating that ~~the~~ method B in which the activation of HA was carried out directly in the presence of the nanoparticles~~,~~ improves cells uptake (Fig. 9B). In contrast, the mean intensity of FITC from the cells incubated with FITC labelled NH_2-MSNs without HA modification is lower and similar for both cell lines. These *in vitro* experiments confirm that MSN/HA can target CD44 over-expressing MDA-MB-231 cancer cells via the HA receptor-mediated endocytosis [84, 86] and phagocytosis [87] pathways, strongly highlighting the potential use of MSN~~s~~/HA as ~~more~~ an efficient approach for tumor-targeting treatments.

Conclusions

MSN/HA samples were prepared following two different conjugation procedures previously reported [36, 37] and using HA of two different molecular weight (6.4 and 200 kDa). The size of HA strongly affects its biological functions and its physico-chemical characteristics [35]. However, to our knowledge this is the first time that such a comparative study is reported, helping the scientific community working in the field to select the best strategy to obtain hybrid nanomaterials with good biological response and potential pharmaceutical applicability. More in detail, our systematic physico-chemical analysis points to the concerted effect of both HA molecular weight and loading ~~on MSN~~ in improving dispersity of MSN. With this respect, we have demonstrated that the 'one pot' method - in which HA is directly activated in the presence of the nanoparticles – is the most efficient, also in terms of possible scale-up.

Our results are also in agreement with recent reports about the importance of considering the interaction of buffer ions with nanoparticles when assessing surface charge and related interphase phenomena, which are of fundamental importance to rationalize results in physiological media [73]. Finally, *in vitro* tests on cancer cell lines demonstrated that MSN/HA are biocompatible and preferentially target cells overexpressing the HA receptor CD44. Also in this context, the best performances are obtained with the 'one pot' sample prepared using HA with high molecular weight (HA200B). All these data suggest the potential use of MSNs/HA as ~~a more~~ efficient approach for tumor-targeting treatments.

Figure captions

Fig. 1 HRTEM images of a) NH_2-MSN; b) HA200A; c) HA200B and d) HA6.4B

Fig. 2 Nitrogen gas-volumetric adsorption (crosses) and desorption (squares) isotherms (top) and pore size distributions (bottom) of a) NH_2-MSN; b) HA200A; c) HA200B and d) HA6.4B

Fig. 3 Infrared spectra in the high and low frequency regions (top and bottom panels, respectively) of NH_2-MSN (black); HA200A (blue); HA200B (red) and HA6.4B (green). Spectra were measured on dehydrated samples and are normalized with respect to pellet thickness

Fig. 4 Water microgravimetric isotherms measured at 28 °C on MSN/HA samples. Top: primary and secondary adsorption/desorption measurements on sample HA6.4B; bottom: comparison of secondary desorption measurements on HA200A (◄), HA200B (■) and HA6.4B (●).

Fig. 5 Dynamic light scattering data of HA200A (blue); HA200B (red) and HA6.4B (green) in PBS measured at 0, 4, 8, 24 and 30 h. The error bars represent the standard deviation of three measurements.

Fig. 6 Images of NH_2-MSN, HA6.4A, HA200A, HA6.4B and HA200B dispersed in PBS with a concentration of 2 mg/ml measured at 0, 4, 8, 24 and 30 h.

Fig. 7 Flow cytometric histograms of CD44 expression in A2780 cells and MDA-MB-231 cells. Red lines: anti-CD44 antibody; blue lines: isotype control.

Fig. 8 Confocal micrographs of A2780 cells (a-c) and MDA-MB-231 cells (d-f) after 24h incubation with different MSN (green fluorescence): NH_2-MSN (a and d), HA6.4B (b and e) and

HA200B (c and f). All MSN are distributed in the cytoplasm but are absent from the nucleus (blue fluorescence). The cytoplasm is counterstained with trypan blue (red fluorescence). Note the higher amount of MSN in e and f. Bars: 10 μm.

Fig. 9 Cellular uptake of FITC labelled NH_2-MSN with or without HA modification in A2780 and MDA-MB-321 cell lines. Analysis of internalization of NH2-MSN, HA6.4B, HA200A and HA200B in A2780 (A) and MDA-MB-231 (B,C) cells by flow cytometry for the indicated time. Data in graphs are expressed as means ± SEM (*$p< 0.05$ and ** $p<0.01$ vs FITC-NH_2-MSN) of three independent experiments.

Fig. 1

1

2

3

4

Fig. 2

5

1

2

3

Fig. 3

1

2

3

4   **Fig. 4**

5

Fig. 5

Fig. 6

1

Median APC-H7		RMFI
Isotype	CD44	
185	201	1,1

A2780

Median APC-H7		RMFI
Isotype	CD44	
239	99279	415

MDA-MB-231

2

3 **Fig. 7**

4

1

NH$_2$-MSN	HA6.4B	HA200B

A2780
cells

MDA-MB-231
cells

2

3   **Fig. 8**
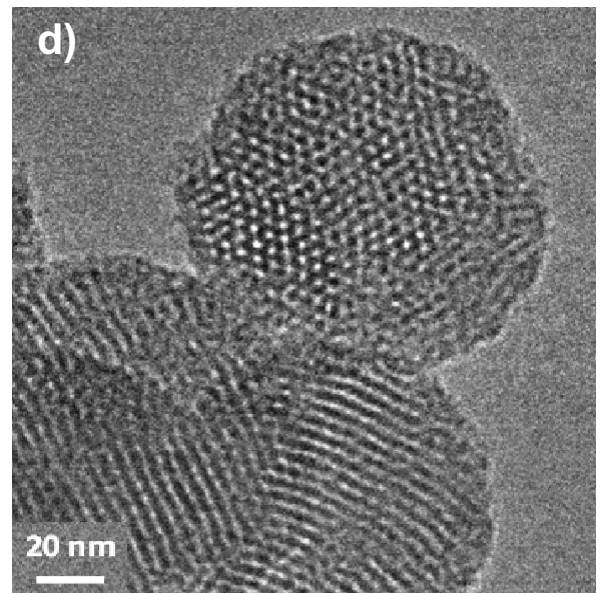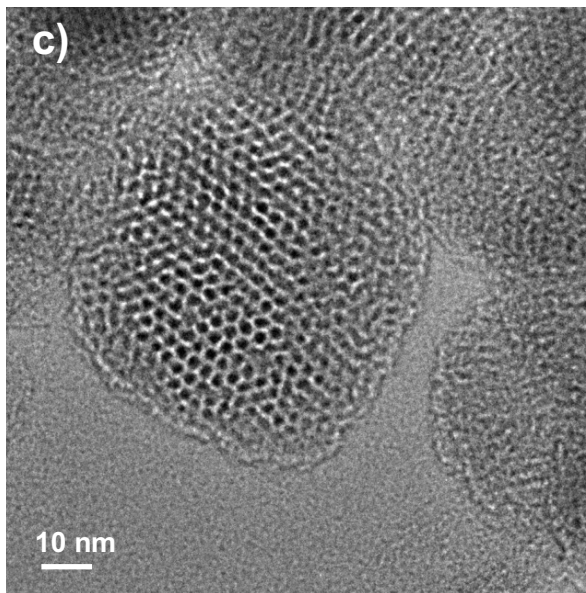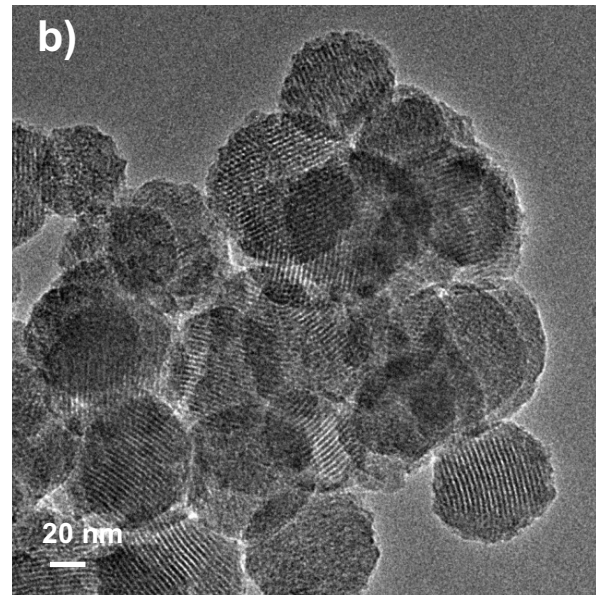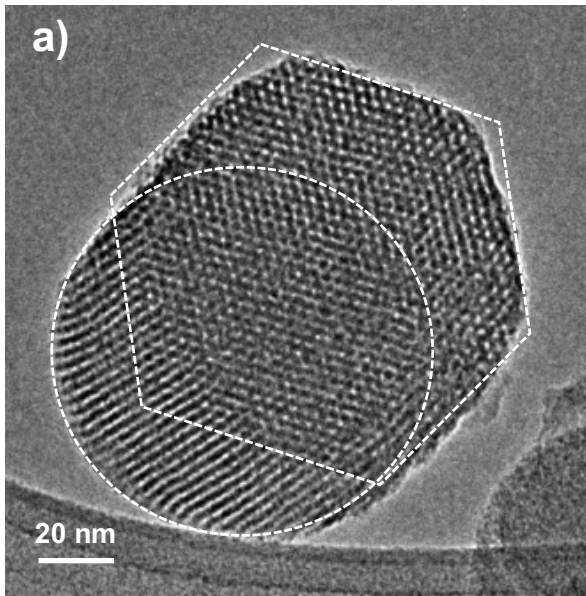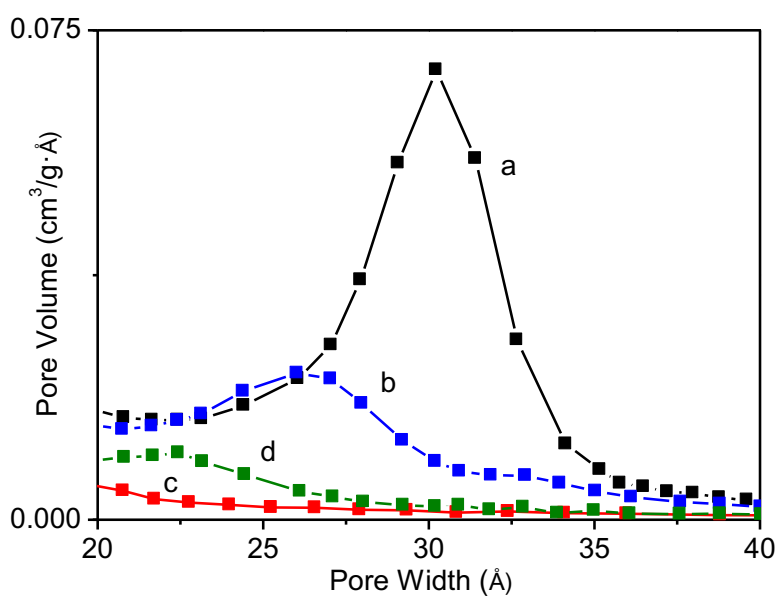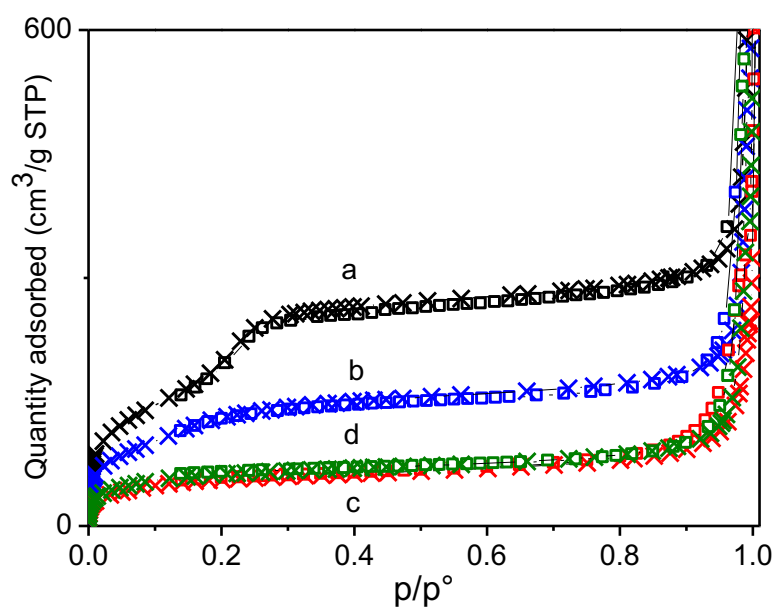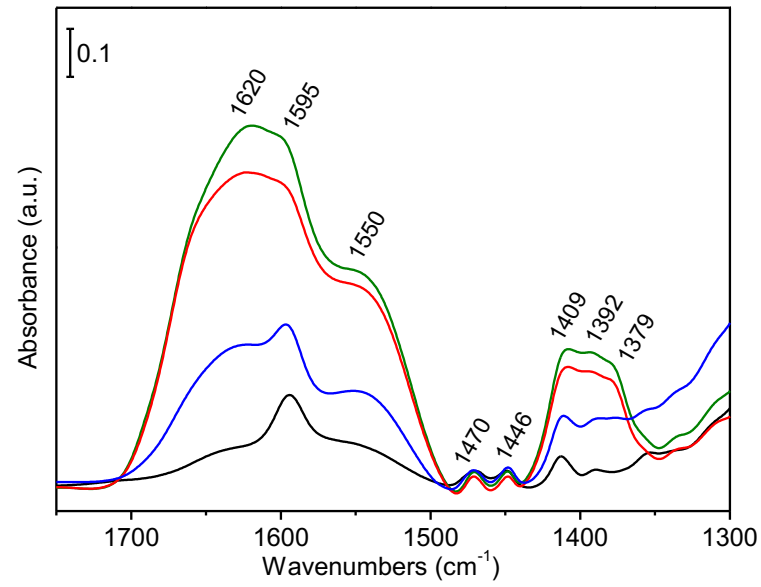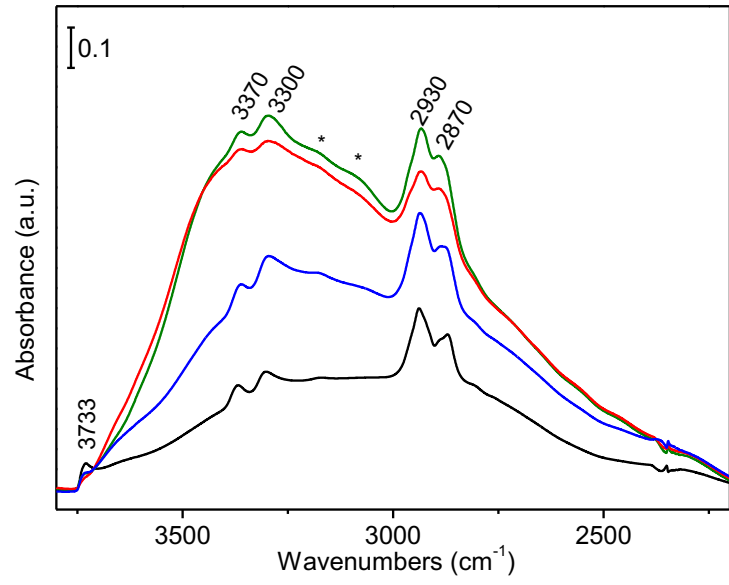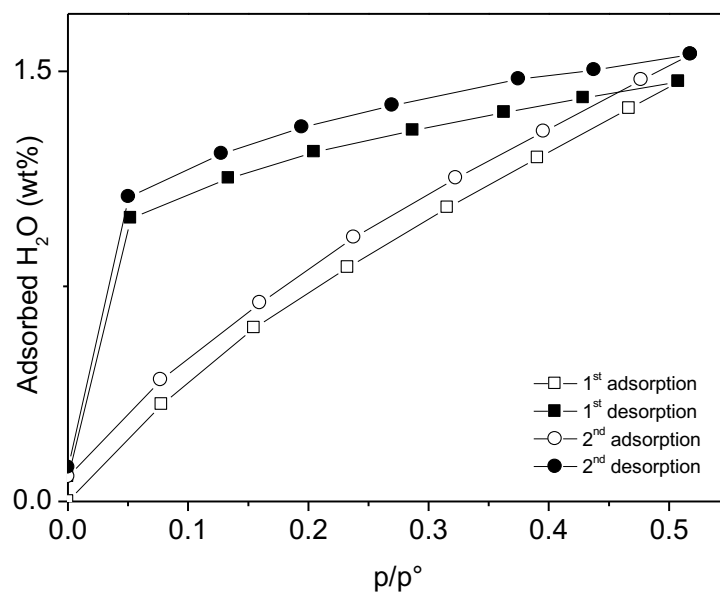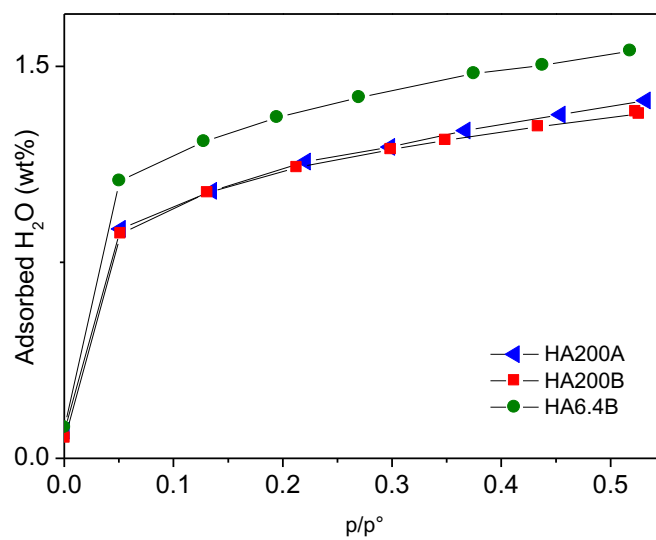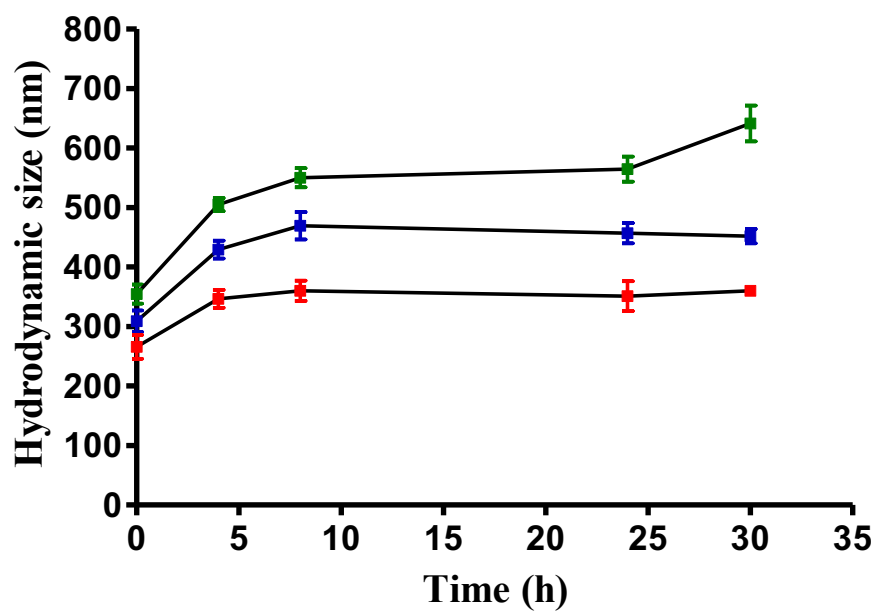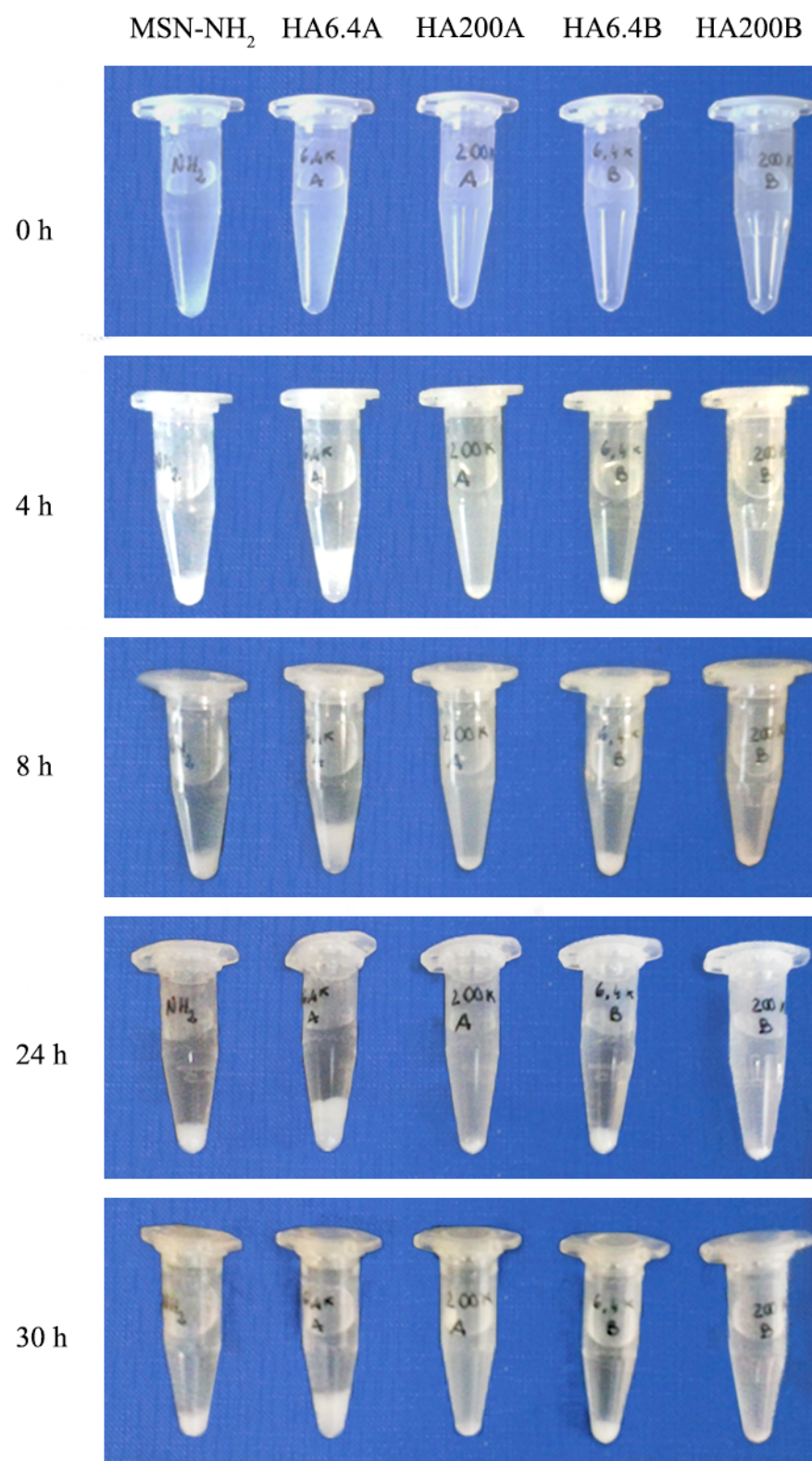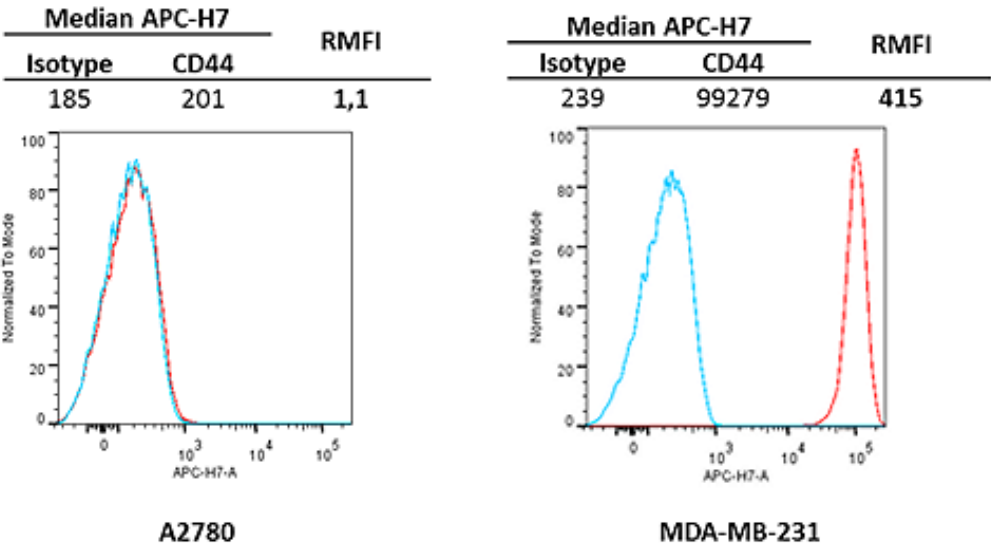
4

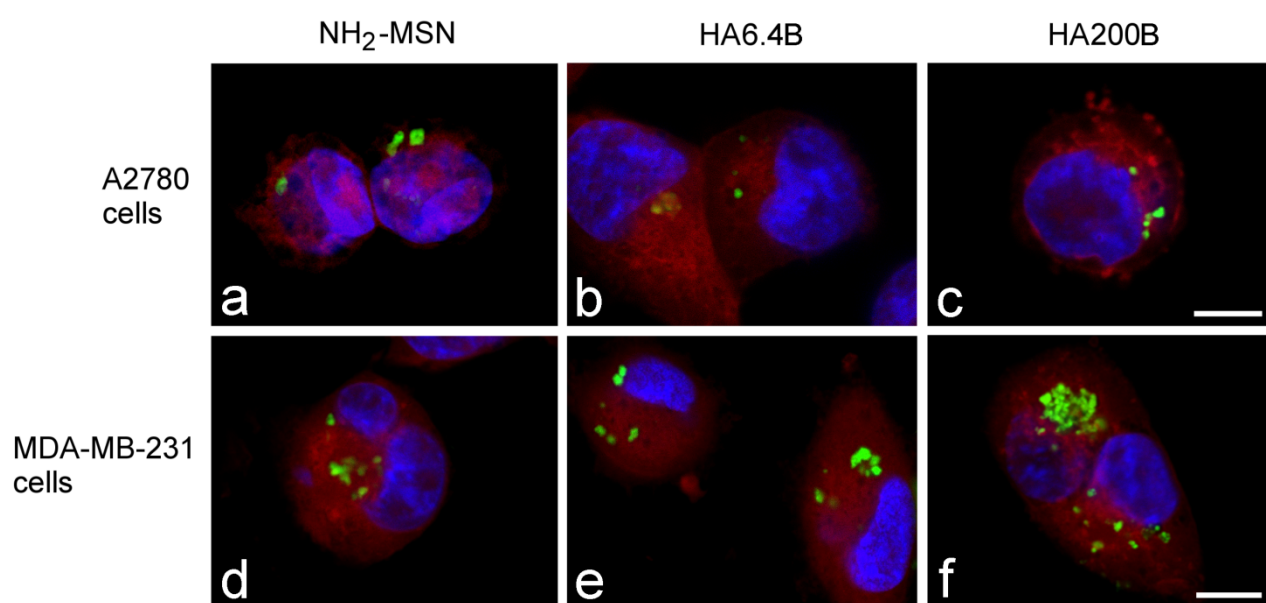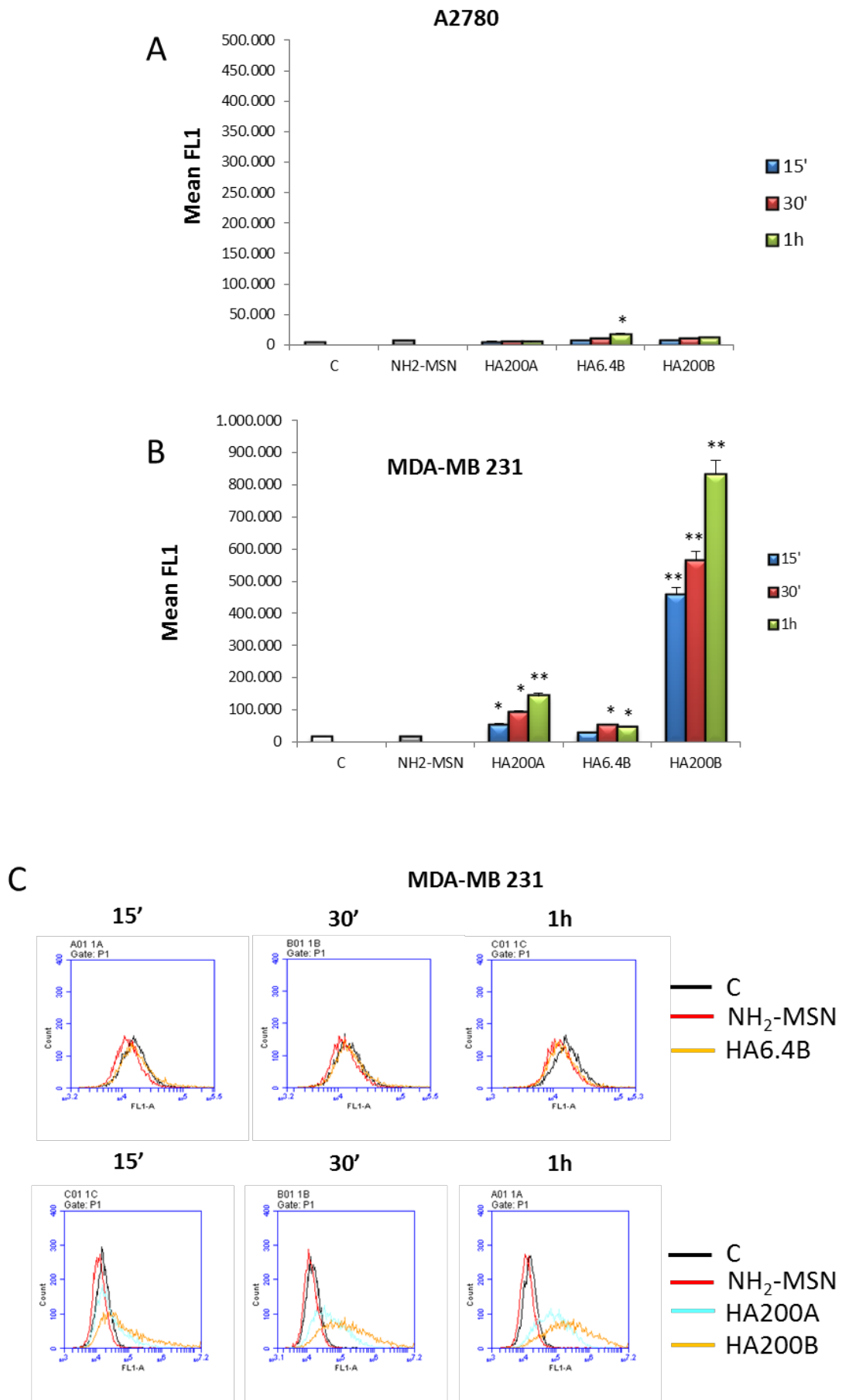**Fig. 9**

Tables

Table 1: Textural and structural properties of the studied materials

Samples	SSA (m²/g)	Mesopores volume (cm³/g)	Mean diameter (Å)	d_{100} (Å)	a (Å)	Wall thickness (Å)
NH$_2$-MSN	789	1.18	30	38.21	44.12	14
HA200A	494	0.91	26	37.88	43.74	18
HA200B	204	0.33	<20	36.32	41.94	>22
HA6.4B	222	0.60	≈22	36.78	42.47	20

Table 2: Quantitative analysis, ~~and~~ ζ potential and mean hydrodynamic diameter

Samples	HA loading (wt%)		ζ potential (mV)		Mean hydrodynamic diameter (nm)	
	TGA	Carbazole	water	PBS[a]	water	PBS[a]
NH$_2$-MSN	-	-	+35.0 ± 0.9	+12.4 ± 0.7	360.7 ± 11.2	409.3 ± 23.0
HA200A	6.6	8.1	+14.3±1.3	-16.5 ± 0.8	292.7 ± 10.6	309.0 ± 18.2
HA200B	17.4	19.9	-19.8 ± 1.9	-15.7 ± 0.9	253.1 ± 10.5	265.9 ± 20
HA6.4A	n. d.	3.1	+34.5 ± 0.1	-1.3 ± 0.5	313.8 ± 8.4	389.2 ± 13.0
HA6.4B	19.0	18.9	-8.8 ± 0.7	-16.8 ± 0.8	301.9 ± 12.1	354.7 ± 16.1

n. d.: not determined; [a] 0.1 M, pH = 7.4

Table 3. Main infrared assignments

High frequency		Low frequency	
Position	Assignment	Position	Assignment
3370 cm^{-1}	ν asym NH$_2$	1650 cm^{-1}	νC=O (Amide I)
3300 cm^{-1}	ν sym NH$_2$	1595 cm^{-1}	δ NH$_2$ (aminoproyl)
2930 cm^{-1}	ν asym CH$_2$	1550 cm^{-1}	δNH/νC-N comb. (Amide II)
2870 cm^{-1}	ν sym CH$_2$	1430-1350 cm^{-1}	δCH and δOH

Table 4: Langmuir parameters for water vapour sorption process

Samples	1st cycle			2nd cycle		
	q$_m$ (wt%)	K	R^2	q$_m$ (wt%)	K	R^2
NH$_2$-MSN [a]	6.83	8.47	0.9267	9.23	8.47	0.9267
HA200A	1.37	17.10	0.9932	1.47	18.29	0.9940
HA200B	1.28	20.14	0.9964	1.43	19.47	0.9964
HA6.4B	1.56	20.87	0.9950	1.66	22.82	0.9968

[a] Parameters calculated from data measured at 25 °C (from Ref. [28])

References

[1] D.J. Irvine, Drug Delivery. One nanoparticle, one kill, Nat. Mater. 10(5) (2011) 342-343.

[2] D. Yohan, B.D. Chithrani, Applications of Nanoparticles in Nanomedicine, J. Biomed. Nanotechnol. 10(9) (2014) 2371-2392.

[3] M. Estanqueiro, M.H. Amaral, J. Conceicao, J.M.S. Lobo, Nanotechnological carriers for cancer chemotherapy: The state of the art, Colloid Surf. B-Biointerfaces 126 (2015) 631-648.

[4] T.M. Sun, Y.S. Zhang, B. Pang, D.C. Hyun, M.X. Yang, Y.N. Xia, Engineered Nanoparticles for Drug Delivery in Cancer Therapy, Angew. Chem. Int. Edit. 53(46) (2014) 12320-12364.

[5] A. Wicki, D. Witzigmann, V. Balasubramanian, J. Huwyler, Nanomedicine in cancer therapy: Challenges, opportunities, and clinical applications, J. Control. Release 200 (2015) 138-157.

[6] R.R. Castillo, M. Colilla, M. Vallet-Regi, Advances in mesoporous silica-based nanocarriers for co-delivery and combination therapy against cancer, Expert Opin. Drug Deliv. 14(2) (2017) 229-243.

[7] X. Sun, Y.P. Luo, L.W. Huang, B.Y. Yu, J.W. Tian, A peptide-decorated and curcumin-loaded mesoporous silica nanomedicine for effectively overcoming multidrug resistance in cancer cells, RSC Adv. 7(27) (2017) 16401-16409.

[8] S. Arpicco, C. Lerda, E.D. Pozza, C. Costanzo, N. Tsapis, B. Stella, M. Donadelli, I. Dando, E. Fattal, L. Cattel, M. Palmieri, Hyaluronic acid-coated liposomes for active targeting of gemcitabine, Eur. J. Pharm. Biopharm. 85(3) (2013) 373-380.

[9] I. Pedrini, E. Gazzano, K. Chegaev, B. Rolando, A. Marengo, J. Kopecka, R. Fruttero, D. Ghigo, S. Arpicco, C. Riganti, Liposomal Nitrooxy-Doxorubicin: One Step over Caelyx in Drug-Resistant Human Cancer Cells, Mol. Pharm. 11(9) (2014) 3068-3079.

[10] B.S. Pattni, V.V. Chupin, V.P. Torchilin, New Developments in Liposomal Drug Delivery, Chem. Rev. 115(19) (2015) 10938-10966.

[11] B. Stella, S. Arpicco, M.T. Peracchia, D. Desmaele, J. Hoebeke, M. Renoir, J. D'Angelo, L. Cattel, P. Couvreur, Design of folic acid-conjugated nanoparticles for drug targeting, J. Pharm. Sci. 89(11) (2000) 1452-1464.

[12] B. Stella, S. Arpicco, F. Rocco, V. Marsaud, J.M. Renoir, L. Cattel, P. Couvreur, Encapsulation of gemcitabine lipophilic derivatives into polycyanoacrylate nanospheres and nanocapsules, Int. J. Pharm. 344(1-2) (2007) 71-77.

[13] B.E. Grottkau, X.X. Cai, J. Wang, X.M. Yang, Y.F. Lin, Polymeric Nanoparticles for a Drug Delivery System, Curr. Drug Metab. 14(8) (2013) 840-846.

[14] I.I. Slowing, J.L. Vivero-Escoto, C.-W. Wu, V.S.Y. Lin, Mesoporous silica nanoparticles as controlled release drug delivery and gene transfection carriers, Adv. Drug Deliv. Rev. 60(11) (2008) 1278-1288.

[15] J. Vivero-Escoto, I. Slowing, B. Trewyn, V. Lin, Mesoporous Silica Nanoparticles for Intracellular Controlled Drug Delivery, Small 18 (2010) 1952-1967.

[16] Y. Chen, H.R. Chen, J.L. Shi, Drug delivery/imaging multifunctionality of mesoporous silica-based composite nanostructures, Expert Opin. Drug Deliv. 11(6) (2014) 917-930.

[17] V. Mamaeva, C. Sahlgren, M. Linden, Mesoporous silica nanoparticles in medicine-Recent advances, Adv. Drug Deliv. Rev. 65(5) (2013) 689-702.

[18] J.M. Rosenholm, V. Mamaeva, C. Sahlgren, M. Linden, Nanoparticles in targeted cancer therapy: mesoporous silica nanoparticles entering preclinical development stage, Nanomedicine 7(1) (2012) 111-120.

[19] H. Meng, M. Xue, J.I. Zink, A.E. Nel, Development of Pharmaceutically Adapted Mesoporous Silica Nanoparticles Platform, J. Phys. Chem. Lett. 3(3) (2012) 358-359.

[20] S.M. Zhu, Z.Y. Zhou, D. Zhang, Control of drug release through the in situ assembly of stimuli-responsive ordered mesoporous silica with magnetic particles, ChemPhysChem 8(17) (2007) 2478-2483.

[21] S.H. Wu, Y.S. Lin, Y. Hung, Y.H. Chou, Y.H. Hsu, C. Chang, C.Y. Mou, Multifunctional mesoporous silica nanoparticles for intracellular labeling and animal magnetic resonance imaging studies, ChemBioChem 9(1) (2008) 53-57.

[22] K.K. Coti, M.E. Belowich, M. Liong, M.W. Ambrogio, Y.A. Lau, H.A. Khatib, J.I. Zink, N.M. Khashab, J.F. Stoddart, Mechanised nanoparticles for drug delivery, Nanoscale 1(1) (2009) 16-39.

[23] Q.F. Zhao, H.J. Geng, Y. Wang, Y.K. Gao, J.H. Huang, Y. Wang, J.H. Zhang, S.L. Wang, Hyaluronic Acid Oligosaccharide Modified Redox-Responsive Mesoporous Silica Nanoparticles for Targeted Drug Delivery, ACS Appl. Mater. Interfaces 6(22) (2014) 20290-20299.

[24] Q.F. Zhao, J. Liu, W.Q. Zhu, C.S. Sun, D.H. Di, Y. Zhang, P. Wang, Z.Y. Wang, S.L. Wang, Dual-stimuli responsive hyaluronic acid-conjugated mesoporous silica for targeted delivery to CD44-overexpressing cancer cells, Acta Biomater. 23 (2015) 147-156.

[25] C. Gimenez, C. de la Torre, M. Gorbe, E. Aznar, F. Sancenon, J.R. Murguia, R. Martinez-Manez, M.D. Marcos, P. Amoros, Gated Mesoporous Silica Nanoparticles for the Controlled Delivery of Drugs in Cancer Cells, Langmuir 31(12) (2015) 3753-3762.

[26] J.H. Zhu, Y.M. Niu, Y. Li, Y.X. Gong, H.H. Shi, Q. Huo, Y. Liu, Q.W. Xu, Stimuli-responsive delivery vehicles based on mesoporous silica nanoparticles: recent advances and challenges, J. Mat. Chem. B 5(7) (2017) 1339-1352.

[27] M. Vallet-Regí, F. Balas, D. Arcos, Mesoporous materials for drug delivery, Angew. Chem. Int. Edit. 46 (2007) 7548-7558.

[28] G.E. Musso, E. Bottinelli, L. Celi, G. Magnacca, G. Berlier, Influence of surface functionalization on the hydrophilic character of mesoporous silica nanoparticles, Phys. Chem. Chem. Phys. 17(21) (2015) 13882-13894.

[29] S.T. Kim, K. Saha, C. Kim, V.M. Rotello, The role of surface functionality in determining nanoparticle cytotoxicity, Acc. Chem. Res. 46(3) (2013) 681-691.

[30] M. Zhu, G. Nie, H. Meng, T. Xia, A. Nel, Y. Zhao, Physicochemical Properties Determine Nanomaterial Cellular Uptake, Transport, and Fate, Acc. Chem. Res. 46(3) (2013) 622-631.

[31] J.L. Townson, Y.-S. Lin, J.O. Agola, E.C. Carnes, H.S. Leong, J.D. Lewis, C.L. Haynes, C.J. Brinker, Re-examining the Size/Charge Paradigm: Differing in Vivo Characteristics of Size- and Charge-Matched Mesoporous Silica Nanoparticles, J. Am. Chem. Soc. 135(43) (2013) 16030-16033.

[32] H. Maeda, Macromolecular therapeutics in cancer treatment: The EPR effect and beyond, J. Control. Release 164(2) (2012) 138-144.

[33] P. Caliceti, S. Salmaso, S. Bersani, Polysaccharide-Based Anticancer Prodrugs, 2010.

[34] S. Arpicco, P. Milla, B. Stella, F. Dosio, Hyaluronic Acid Conjugates as Vectors for the Active Targeting of Drugs, Genes and Nanocomposites in Cancer Treatment, Molecules 19(3) (2014) 3193-3230.

[35] F. Dosio, S. Arpicco, B. Stella, E. Fattal, Hyaluronic acid for anticancer drug and nucleic acid delivery, Adv. Drug Deliv. Rev. 97 (2016) 204-236.

[36] M. Ma, H.R. Chen, Y. Chen, K. Zhang, X. Wang, X.Z. Cui, J.L. Shi, Hyaluronic acid-conjugated mesoporous silica nanoparticles: excellent colloidal dispersity in physiological fluids and targeting efficacy, J. Mater. Chem. 22(12) (2012) 5615-5621.

[37] M.H. Yu, S. Jambhrunkar, P. Thorn, J.Z. Chen, W.Y. Gu, C.Z. Yu, Hyaluronic acid modified mesoporous silica nanoparticles for targeted drug delivery to CD44-overexpressing cancer cells, Nanoscale 5(1) (2013) 178-183.

[38] A. Salis, M. Fanti, L. Medda, V. Nairi, F. Cugia, M. Piludu, V. Sogos, M. Monduzzi, Mesoporous Silica Nanoparticles Functionalized with Hyaluronic Acid and Chitosan Biopolymers. Effect of Functionalization on Cell Internalization, ACS Biomater. Sci. Eng. 2(5) (2016) 741-751.

[39] M.Z. Zhang, C.L. Xu, L.Q. Wen, M.K. Han, B. Xiao, J. Zhou, Y.C. Zhang, Z. Zhang, E. Viennois, D. Merlin, A Hyaluronidase-Responsive Nanoparticle-Based Drug Delivery System for Targeting Colon Cancer Cells, Cancer Res. 76(24) (2016) 7208-7218.

[40] Z.W. Chen, Z.H. Li, Y.H. Lin, M.L. Yin, J.S. Ren, X.G. Qu, Bioresponsive Hyaluronic Acid-Capped Mesoporous Silica Nanoparticles for Targeted Drug Delivery, Chem. Euro J. 19(5) (2013) 1778-1783.

[41] L. Chen, X.J. Zhou, W. Nie, Q.Q. Zhang, W.Z. Wang, Y.Z. Zhang, C.L. He, Multifunctional Redox-Responsive Mesoporous Silica Nanoparticles for Efficient Targeting Drug Delivery and Magnetic Resonance Imaging, ACS Appl. Mater. Interfaces 8(49) (2016) 33829-33841.

[42] D. Tarn, M. Xue, J.I. Zink, pH-Responsive Dual Cargo Delivery from Mesoporous Silica Nanoparticles with a Metal-Latched Nanogate, Inorg. Chem. 52(4) (2013) 2044-9.

[43] D.R. Radu, C.Y. Lai, K. Jeftinija, E.W. Rowe, S. Jeftinija, V.S.Y. Lin, A polyamidoamine dendrimer-capped mesoporous silica nanosphere-based gene transfection reagent, J. Am. Chem. Soc. 126 (2004) 13216-13217.

[44] K.M. Parida, D. Rath, Amine functionalized MCM-41: An active and reusable catalyst for Knoevenagel condensation reaction, J. Mol. Catal. A -Chem. 310(1-2) (2009) 93-100.

[45] P. Iliade, I. Miletto, S. Coluccia, G. Berlier, Functionalization of mesoporous MCM-41 with aminopropyl groups by co-condensation and grafting: a physico-chemical characterization, Res. Chem. Intermed. 38 (2012) 785-794.

[46] K.C. Vrancken, K. Possemiers, P. Vandervoort, E.F. Vansant, Surface modification of silica-gels with aminoorganosilanes, Colloid Surf. A 98(3) (1995) 235-241.

[47] T. Bitter, H.M. Muir, A modified uronic acid carbazole reaction, Anal. Biochem. 4(4) (1962) 330-334.

[48] F. Rouquerol, J. Rouquerol, K. Sing, Adsorption by Powders & Porous Solids, Academic press1999.

[49] V. Vichai, K. Kirtikara, Sulforhodamine B colorimetric assay for cytotoxicity screening, Nat. Protoc. 1 (2006) 1112–1116.

[50] S. Sapino, E. Ugazio, L. Gastaldi, I. Miletto, G. Berlier, D. Zonari, S. Oliaro-Bosso, Mesoporous silica as topical nanocarriers for quercetin: characterization and in vitro studies, Eur. J. Pharm. Biopharm. 89 (2015) 116-125.

[51] A. Malfanti, I. Miletto, E. Bottinelli, D. Zonari, G. Blandino, G. Berlier, S. Arpicco, Delivery of Gemcitabine Prodrugs Employing Mesoporous Silica Nanoparticles, Molecules 21(4) (2016).

[52] R. Mellaerts, M.B.J. Roeffaers, K. Houthoofd, M. Van Speybroeck, G. De Cremer, J.A.G. Jammaer, G. Van den Mooter, P. Augustijns, J. Hofkens, J.A. Martens, Molecular organization of hydrophobic molecules and co-adsorbed water in SBA-15 ordered mesoporous silica material, Phys. Chem. Chem. Phys. 13(7) (2011) 2706-2713.

[53] R. Mellaerts, E.J. Fayad, G. Van den Mooter, P. Augustijns, M. Rivallan, F. Thibault-Starzyk, J.A. Martens, In Situ FT-IR Investigation of Etravirine Speciation in Pores of SBA-15 Ordered Mesoporous Silica Material upon Contact with Water, Mol. Pharm. 10(2) (2013) 567-573.

[54] L. Medda, M.F. Casula, M. Monduzzi, A. Salis, Adsorption of Lysozyme on Hyaluronic Acid Functionalized SBA-15 Mesoporous Silica: A Possible Bioadhesive Depot System, Langmuir 30(43) (2014) 12996-13004.

[55] M. Halo, A.M. Ferrari, G. Berlier, I. Miletto, S. Casassa, Experimental and first-principles IR characterization of quercetin adsorbed on a silica surface, Theor. Chem. Acc. 135(5) (2016).

[56] R. Onnainty, B. Onida, P. Paez, M. Longhi, A. Barresi, G. Granero, Targeted chitosan-based bionanocomposites for controlled oral mucosal delivery of chlorhexidine, Int. J. Pharm. 509(1-2) (2016) 408-418.

[57] G. Paul, G.E. Musso, E. Bottinelli, M. Cossi, L. Marchese, G. Berlier, Investigating the interaction of water vapour with aminopropyl groups on the surface of mesoporous silica nanoparticles, ChemPhysChem 18 (2017) 839-849.

[58] V. Nairi, L. Medda, M. Monduzzi, A. Salis, Adsorption and release of ampicillin antibiotic from ordered mesoporous silica, J. Colloid Interface Sci. 497 (2017) 217-225.

[59] A. Weeks, D. Luensmann, A. Boone, L. Jones, H. Sheardown, Hyaluronic acid as an internal wetting agent in model DMAA/TRIS contact lenses, J. Biomater. Appl. 27(4) (2012) 423-432.

[60] A. Weeks, D. Morrison, J.G. Alauzun, M.A. Brook, L. Jones, H. Sheardown, Photocrosslinkable hyaluronic acid as an internal wetting agent in model conventional and silicone hydrogel contact lenses, J. Biomed. Mater. Res. Part A 100A(8) (2012) 1972-1982.

[61] A. Weeks, L.N. Subbaraman, L. Jones, H. Sheardown, The Competing Effects of Hyaluronic and Methacrylic Acid in Model Contact Lenses, Journal of Biomaterials Science-Polymer Edition 23(8) (2012) 1021-1038.

[62] Y.J. Wang, L. Guo, L. Ren, S.H. Yin, J. Ge, Q.Y. Gao, T. Luxbacher, S.J. Luo, A study on the performance of hyaluronic acid immobilized chitosan film, Biomed. Mater. 4(3) (2009).

[63] C.A. Acevedo, E. Sanchez, P. Diaz-Calderon, J.J. Blaker, J. Enrione, F. Quero, Synergistic effects of crosslinking and chitosan molecular weight on the microstructure, molecular mobility, thermal and sorption properties of porous chitosan/gelatin/hyaluronic acid scaffolds, J. Appl. Polym. Sci. 134(18) (2017).

[64] R.L. Huang, X. Liu, H.J. Ye, R.X. Su, W. Qi, L.B. Wang, Z.M. He, Conjugation of Hyaluronic Acid onto Surfaces via the Interfacial Polymerization of Dopamine to Prevent Protein Adsorption, Langmuir 31(44) (2015) 12061-12070.

[65] X. Liu, R.L. Huang, R.X. Su, W. Qi, L.B. Wang, Z.M. He, Grafting Hyaluronic Acid onto Gold Surface to Achieve Low Protein Fouling in Surface Plasmon Resonance Biosensors, ACS Appl. Mater. Interfaces 6(15) (2014) 13034-13042.

[66] M.A.J. Mazumder, Polydimethylsiloxane Substrates with Surfaces Decorated by Immobilized Hyaluronic Acids of Different Molecular Weight for Biomedical Applications, Arab. J. Sci. Eng. 42(1) (2017) 271-280.

[67] M.H. Ramadan, J.E. Prata, O. Karacsony, G. Duner, N.R. Washburn, Reducing Protein Adsorption with Polymer-Grafted Hyaluronic Acid Coatings, Langmuir 30(25) (2014) 7485-7495.

[68] M. Van Beek, A. Weeks, L. Jones, H. Sheardown, Immobilized hyaluronic acid containing model silicone hydrogels reduce protein adsorption, Journal of Biomaterials Science-Polymer Edition 19(11) (2008) 1425-1436.

[69] M. Morga, Z. Adamczyk, D. Kosior, Silica nanoparticle monolayers on a macroion modified surface: formation mechanism and stability, Phys. Chem. Chem. Phys. 19(34) (2017) 22721-22732.

[70] M. Colilla, I. Izquierdo-Barba, S. Sanchez-Salcedo, J.L.G. Fierro, J.L. Hueso, M. Vallet-Regí, Synthesis and Characterization of Zwitterionic SBA-15 Nanostructured Materials, Chem. Mater. 22(23) (2010) 6459-6466.

[71] J.M. Rosenholm, M. Linden, Towards establishing structure-activity relationships for mesoporous silica in drug delivery applications, J. Control. Release 128(2) (2008) 157-164.

[72] C. Giaveno, L. Celi, R.M. Aveiro Cessa, M. Prati, E. Bonifacio, E. Barberis, Interaction of organic phosphorus with clays extracted from Oxisols, Soil Sci. 173 (2008) 694-706.

[73] F. Cugia, S. Sedda, F. Pitzalis, D.F. Parsons, M. Monduzzi, A. Salis, Are specific buffer effects the new frontier of Hofmeister phenomena? Insights from lysozyme adsorption on ordered mesoporous silica, RSC Adv. 6(97) (2016) 94617-94621.

[74] M. Etienne, S. Goubert-Renaudin, Y. Rousselin, C. Marichal, F. Denat, B. Lebeau, A. Walcarius, Multiarm Cyclam-Grafted Mesoporous Silica: A Strategy to Improve the Chemical Stability of Silica Materials Functionalized with Amine Ligands, Langmuir 25(5) (2009) 3137-3145.

[75] M. Etienne, A. Walcarius, Analytical investigation of the chemical reactivity and stability of aminopropyl-grafted silica in aqueous medium, Talanta 59(6) (2003) 1173-1188.

[76] A. Walcarius, M. Etienne, B. Lebeau, Rate of access to the binding sites in organically modified silicates. 2. Ordered mesoporous silicas grafted with amine or thiol groups, Chem. Mater. 15(11) (2003) 2161-2173.

[77] M. Morga, Z. Adamczyk, Monolayers of cationic polyelectrolytes on mica - Electrokinetic studies, J. Colloid Interface Sci. 407 (2013) 196-204.

[78] Y. Tataurova, M.J. Sealy, R.G. Larsen, S.C. Larsen, Surface-Selective Solution NMR Studies of Functionalized Zeolite Nanoparticles, J. Phys. Chem. Lett. 3(3) (2012) 425-429.

[79] A. Marucco, F. Catalano, I. Fenoglio, F. Turci, G. Martra, B. Fubini, Possible Chemical Source of Discrepancy between in Vitro and in Vivo Tests in Nanotoxicology Caused by Strong Adsorption of Buffer Components, Chem. Res. Toxicol. 28(1) (2015) 87-91.

[80] M. Morga, A. Michna, Z. Adamczyk, Formation and stability of polyelectrolyte/polypeptide monolayers determined by electrokinetic measurements, Colloid Surf. A 529 (2017) 302-310.

[81] R.J.S. Sneath, D.C. Mangham, The normal structure and function of CD44 and its role in neoplasia, J. Clin. Pathol.-Mol. Pathol. 51 (1998) 191-200.

[82] M. Costanzo, F. Carton, A. Marengo, G. Berlier, B. Stella, S. Arpicco, M. Malatesta, Fluorescence and electron microscopy to visualize the intracellular fate of nanoparticles for drug delivery, Eur. J. Histochem. 60(2) (2016) 107-115.

[83] Z.W. Chen, Z.H. Li, Y.H. Lin, M.L. Yin, J.S. Ren, X.G. Qu, Biomineralization inspired surface engineering of nanocarriers for pH-responsive, targeted drug delivery, Biomaterials 34(4) (2013) 1364-1371.

[84] M. El-Dakdouki, E. Puré, X. Huang, Development of drug loaded nanoparticles for tumor targeting. Part 1: synthesis, characterization, and biological evaluation in 2D cell cultures, Nanoscale (5) (2013) 3895-3903.

[85] S. Poussard, M. Decossas, O. Le Bihan, S. Mornet, G. Naudin, O. Lambert, Internalization and fate of silica nanoparticles in C2C12 skeletal muscle cells: evidence of a beneficial effect on myoblast fusion, Int. J. Nanomed. 10 (2015) 1479-1492.

[86] R. Racine, M.E. Mummert, Hyaluronan Endocytosis: Mechanisms of Uptake and Biological Functions, Molecular Regulation of Endocytosis (2012) 377-390.

[87] P.P. Ostrowski, S. Grinstein, S.A. Freeman, Diffusion Barriers, Mechanical Forces, and the Biophysics of Phagocytosis, Dev. Cell 38(2) (2016) 135-146.